RSC Publishing Faraday Discussions

Decomposing Electronic and Lattice Contributions in Optical Pump–X-ray Probe Transient Inner-Shell Absorption Spectroscopy of CuO

Journal:	*Faraday Discussions*
Manuscript ID	FD-ART-12-2018-000236.R1
Article Type:	Paper
Date Submitted by the Author:	24-Dec-2018

Complete List of Authors:	Mahl, Johannes; Lawrence Berkeley National Laboratory, Chemical Sciences Division; Universitat Hamburg, Physics Department Neppl, Stefan; Lawrence Berkeley National Laboratory, Chemical Sciences; Helmholtz-Zentrum Berlin fur Materialien und Energie GmbH Roth, Friedrich; Technische Universitat Bergakademie Freiberg; Center for Free-Electron Laser Science DESY Borgwardt, Mario; Lawrence Berkeley National Laboratory, Chemical Sciences Division Saladrigas, Catherine; Lawrence Berkeley National Laboratory, Chemical Sciences Division; University of California, Berkeley, Chemistry Toulson, Benjamin; Lawrence Berkeley National Laboratory, Chemical Sciences Division Cooper, Jason; Lawrence Berkeley National Lab, JCAP Rahman, Tahiyat; Lawrence Berkeley National Laboratory, Chemical Sciences Division Bluhm, Hendrik; Lawrence Berkeley National Laboratory, Chemical Sciences Division and Advanced Light Source; Guo, Jinghua; Lawrence Berkeley National Laboratory, Yang, Wanli; Lawrence Berkeley National Laboratory, Advanced Light Source Huse, Nils; University of Hamburg, Department of Physics Eberhardt, Wolfgang; IOAP, Gessner, Oliver; Lawrence Berkeley National Laboratory, Chemical Sciences Division

Ultrafast Photoinduced Energy and Charge Transfer

ARTICLE

Decomposing Electronic and Lattice Contributions in Optical Pump – X-ray Probe Transient Inner-Shell Absorption Spectroscopy of CuO

Received 00th January 20xx,
Accepted 00th January 20xx

DOI: 10.1039/x0xx00000x

www.rsc.org/

Johannes Mahl[a,b], Stefan Neppl[a,c], Friedrich Roth[d,e], Mario Borgwardt[a], Catherine Saladrigas[a,f], Benjamin Toulson[a], Jason Cooper[g], Tahiyat Rahman[a], Hendrik Bluhm[a,h], Jinghua Guo[h], Wanli Yang[h], Nils Huse[b,e], Wolfgang Eberhardt[e,h], and Oliver Gessner[a]

Electronic and lattice contributions to picosecond time-resolved X-ray absorption spectra (trXAS) of CuO at the oxygen K-edge are analyzed by comparing trXAS spectra, recorded using excitation wavelengths of 355 nm and 532 nm, to steady-state, temperature-dependent XAS measurements. The trXAS spectra at pump-probe time-delays ≥150 ps are dominated by lattice heating effects. Insight into the temporal evolution of lattice temperature profiles on timescales up to 100's of nanoseconds after laser excitation are reported, on an absolute temperature scale, with a temporal sensitivity and a spatial selectivity on the order of 10's of picoseconds and 10's of nanometers, respectively, effectively establishing an "ultrafast thermometer". In particular, for the 532 nm experiment at ~5 mJ/cm² fluence, both the initial sample temperature and its dynamic evolution are well captured by a one-dimensional thermal energy deposition and diffusion model. The thermal conductivity k = (1.3±0.4) W m^{-1} K^{-1} derived from this model is in good agreement with the literature value for CuO powder k_{powder} = 1.013 W m^{-1} K^{-1}. For 355 nm excitation, a quantitative analysis of the experiments is hampered by the large temperature gradients within the probed sample volume owing to the small UV penetration depth. The impact of the findings on mitigating or utilizing photoinduced lattice temperature changes in future X-ray free electron laser (XFEL) experiments is discussed.

[a] Chemical Sciences Division, Lawrence Berkeley National Laboratory, Berkeley, California, USA
[b] Physics Department Universität Hamburg, Hamburg, Germany
[c] Present Address: Helmholtz-Zentrum Berlin für Materialien und Energie, Berlin, Germany
[d] Institute for Experimental Physics, TU Bergakademie Freiberg, Germany
[e] Center for Free-Electron Laser Science DESY, Hamburg, Germany
[f] Department of Chemistry, University of California, Berkeley, California, USA
[g] Joint Center for Artificial Photosynthesis, Lawrence Berkeley National Laboratory, Berkeley, California, USA
[h] Advanced Light Source, Lawrence Berkeley National Laboratory, Berkeley, California, USA

Ultrafast Photoinduced Energy and Charge Transfer

ARTICLE

1. Introduction

As research in the field of ultrafast X-ray science progresses toward the use of high repetition rate X-ray free-electron lasers[1,2] and high-order harmonic generation (HHG) light sources,[3,4] it is crucial to understand the impact of corresponding high-repetition rate excitation processes on non-replenishing samples that are typical for many applications in materials and chemical sciences. Thermal excitations including phase transitions and their X-ray spectroscopic fingerprints play a particularly important role as they are a ubiquitous, often unintended consequence of virtually all photon absorption processes in condensed phase materials through coupling of electronic and nuclear motion. Understanding and, in many cases, mitigating the impact of thermal excitations on ultrafast X-ray spectroscopy and scattering signals is crucial for the success of a large range of experiments. This applies, in particular, to dynamics that are strongly coupled to thermal excitations[5] and/or that extend beyond the first ~100 fs after photoexcitation where signal contributions from lattice motion due to electron-phonon coupling may become relevant.[6] Despite their importance, systematic studies of the relative contributions and dynamic trends of electronic and lattice excitations in time-resolved X-ray spectroscopy data are scarce to date. Hayes et al. found that photoinduced changes in the iron K-edge X-ray absorption spectrum of hematite (α-Fe_2O_3), recorded 100 ps after super-bandgap excitation with 3.5 eV photons, are entirely dominated by lattice heating effects.[7] Lin et al. used femtosecond time-resolved XUV absorption spectroscopy to investigate photoinduced dynamics in PbI_2.[8] The transient XUV spectra in this study are well reproduced by lattice temperature dependent changes for pump-probe delays greater than ~4 ps. In an attosecond time-resolved XUV transient absorption experiment on silicon, Schultze et al. observed lattice-motion induced band-gap modifications as early as ~60 fs after photoexcitation.[6] Evidently, signal contributions due to lattice motion are an integral part of time-resolved X-ray spectroscopy that can have decisive impact on the feasibility of experiments. It is essential to characterize these signal contributions and to understand their dynamics based on the underlying physics.

Here, we study photoinduced dynamics in the transition metal oxide semiconductor CuO (cupric oxide) using picosecond time-resolved laser-pump – X-ray-probe transient absorption spectroscopy (trXAS). CuO is a p-type semiconductor with possible applications in photocatalytic degradation of organic pollutants,[9,10] hydrogen production from water,[11–13] and as anode material in lithium batteries.[14] In many of these applications, CuO is used in conjunction with wide band gap semiconductors, such as ZnO and TiO_2, to cover a large portion of the solar spectrum. In the experiments presented here, we study a CuO film that is generated by thermal surface oxidation of a sheet of copper. The trXAS experiments are performed at the oxygen K-edge near ~540 eV using a previously described optical-pump – X-ray-probe picosecond trXAS setup at beamline 8 of the Advanced Light Source (ALS).[15] The pump pulse repetition rate of 127 kHz is comparable to the current 100 kHz design target for the first stage of the Linac Coherent Light Source upgrade (LCLS II). Pump-probe experiments are performed at two different photon energies of 2.33 eV and 3.49 eV. Band gap values for CuO have been reported across a range of ~1.0-2.1 eV,[16–23] thus, both laser wavelengths induce super-bandgap excitations. Relaxation to the conduction band minimum via electron-phonon coupling occurs on timescales much smaller than the 70 ps time resolution of the experiment. Therefore, the main difference between measurements with the two different wavelengths is the transfer of an additional 1.2 eV into phonons before relaxation across the band gap, i.e., a potentially higher lattice temperature after excitation with 355 nm, assuming the same number of excitations per unit sample volume. Thus, comparing measurements for both excitation wavelengths a) using the same excitation density and b) using the same total excitation energy (photon energy × excitation density) provides insight into the relative impact of electronic and lattice contributions to the trXAS spectra. Relaxation dynamics are monitored across a pump-probe time-delay range of ~350 ns.

The time-dependent optical-pump – X-ray-probe experiments are complemented by steady-state, temperature-dependent XAS (XAS_{temp}) measurements at sample temperatures between 22˚C and 145˚C, providing a reference for purely temperature-induced effects. The photoinduced changes in the CuO oxygen K-edge trXAS spectra recorded ≥150 ps after photoexcitation with either 355 nm or 532 nm are well reproduced by effects due to increased lattice temperatures. The XAS_{temp} measurements are used to create a "temperature ruler" for the trXAS data, yielding picosecond-time resolved lattice temperature trends. Temperatures for both excitation wavelengths at comparable pump laser fluences of ~5 mJ/cm^2 exhibit an initial fast decay within ~10's of nanoseconds, followed by a slower cooling trend on ~100's of nanosecond timescales. These dynamics are well reproduced by a one-dimensional thermal diffusion model that explicitly takes into account the depth-dependent intensity distributions of both the

UV/vis pump pulses as well as the X-ray probe pulse. Comparison of the 355 nm and 532 nm results illustrates that a detailed modeling of these depth-dependent intensity profiles is crucial for a quantitative understanding of the physics underlying the laser-induced heating and subsequent cooling processes and their impact on the recorded trXAS spectra. The measurements yield a thermal conductivity of the CuO film of k = (1.3±0.4) W m^{-1} K^{-1}, which is in good agreement with the literature value for CuO powder 1.013 W m^{-1} K^{-1} in ref. 24 and approximately an order of magnitude smaller than the smallest literature value for bulk CuO 18 W m^{-1} K^{-1} in ref. 25. The findings are rationalized by surface morphology modifications during the sample preparation by thermal annealing, which have previously been documented by temperature-dependent atomic force microscopy (AFM).[26]

2. Experimental details

2.1 Time-resolved XAS For the trXAS experiment, a mobile laser-pump – X-ray-probe setup is employed at beamline 8.0.1.2 of the ALS. The setup and its operation have previously been described in detail.[15] Briefly, CuO samples are excited with 10 ps full-width-at-half-maximum (FWHM) laser pulses of either 532 nm (2.33 eV) or 355 nm (3.49 eV) wavelength (photon energy) and interrogated with 70 ps long X-ray pulses from the ALS. Time-dependent oxygen K-edge absorption spectra are recorded in total fluorescence yield (TFY) mode with a time-sensitive micro-channel plate detector.[27] The detector is capable of distinguishing TFY signals from individual ALS pulses, enabling the simultaneous recording of trXAS spectra at multiple laser-pump – X-ray-probe time delays. The laser system is synchronized to the ALS and operated at ~127 kHz repetition rate. Excited state spectra ("pumped") are compared to ground state reference spectra ("unpumped") by creating difference spectra for each pump-probe delay, ΔtrXAS(Δt) = trXAS$_{pumped}$(Δt) - trXAS$_{unpumped}$. The sample is raster-scanned with 250 µm/s scan speed and a 500 µm spacing between neighboring lines to mediate sample damage and thermally induced phase transitions.

2.2 Selection of pump laser fluences Experiments are performed using pump laser photon energies (wavelengths) of 3.49 eV (λ=355 nm) and 2.33 eV (λ=532 nm), both of which are beyond the band gap of CuO (≈1.0-2.1 eV[16–23]). For each laser wavelength, measurements are performed at two different fluences, 2.7 mJ/cm^2 and 4.6 mJ/cm^2 for 355 nm as well as 1.7 mJ/cm^2 and 4.8 mJ/cm^2 for 532 nm. Fluences are estimated based on the assumption that the FWHM laser focus area contains 50% of the pulse energy. The two higher fluence values are chosen such that both the fluence and the total energy deposited in the sample are the same at each laser wavelength (with the laser spot sizes approximately the same for both colors). The 2.7 mJ/cm^2 fluence for 355 nm excitation is chosen such that the average laser excitation density within the probed volume is expected to be comparable to that for 532 nm and 4.8 mJ/cm^2. The measurement with 1.7 mJ/cm^2 fluence at 532 nm pump wavelength has been performed as an additional reference point to gauge the impact of the laser fluence on the sample response.

2.3 Temperature-resolved XAS The trXAS measurements are complemented by temperature-dependent X-ray absorption spectra (XAS$_{temp}$) recorded at ALS beamline 11.0.2. The XAS$_{temp}$ spectra are acquired in TFY mode using a photodiode covered with an Al filter to suppress background signals from ambient light. The sample is mounted on a button heater stage to control the sample temperature, which is monitored with a thermocouple attached to the front side of the sample. All measurements are performed under 3 mTorr of oxygen, in order to increase the temperature at which the phase transition of CuO to Cu_2O starts to occur.[28,29] Temperature-induced difference spectra ΔXAS$_{temp}$ are calculated by subtracting room temperature (RT) spectra from spectra acquired at elevated temperatures ΔXAS$_{temp}$($\Delta T = T–RT$) = XAS$_{temp}$(T) – XAS$_{temp}$(RT). For direct comparison of the ΔXAS$_{temp}$(ΔT) and the ΔtrXAS(Δt) spectra, RT = 28°C was used as prolonged laser exposure leads to a slightly increased equilibrium temperature of the sample (see section 4 for details).

Further details on the sample preparation, trXAS technique, and choice of pump laser fluences are given in the Supplementary Information (SI).

3. Results

Fig. 1a shows static X-ray absorption spectra acquired in total fluorescence yield (TFY, black) and total electron yield (TEY, blue) mode. The spectra agree well with TEY measurements by Jiang et al., shown in red.[30] For comparison, the Cu_2O spectrum from the same study is also included (gray, dashed). The absence of the main Cu_2O resonance feature at 532.5 eV in the black and blue spectra indicates a high purity of the prepared CuO film. The slightly better agreement, concerning the amplitude, between the TEY spectra compared to the TFY spectrum is likely due to saturation and self-absorption effects in the TFY signal.[31] These are minimized by choosing a geometry with a normal X-ray incidence angle and grazing angle X-ray fluorescence detection (~0° and ~80°, respectively, relative to the sample surface normal). Fig. 1b shows static TFY spectra from all samples used for the time-resolved measurements presented here, demonstrating very good reproducibility of the sample preparation and experimental conditions. All spectra are normalized to the same increase between pre- and post-edge signals.

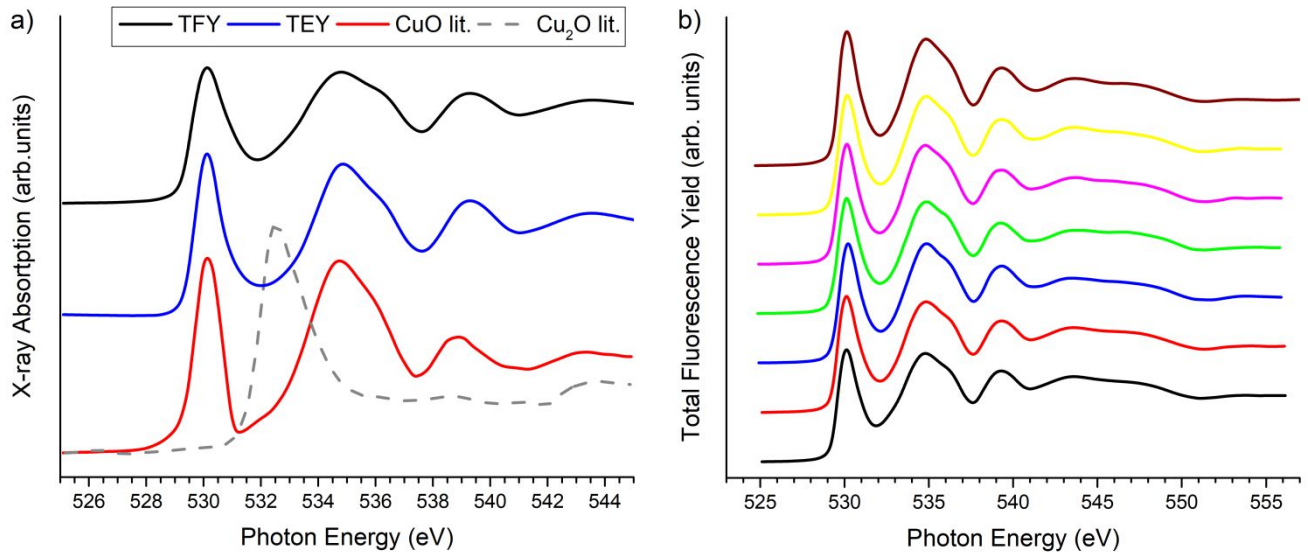

Fig. 1. a) Comparison of static oxygen K-edge XAS spectra of CuO acquired in TFY (black) and TEY (blue) mode with CuO (red) and Cu_2O (gray, dashed) reference spectra from Jiang et al.[30] b) Static TFY spectra from all samples used for time-resolved measurements. Spectra in a) and b) have been offset vertically for improved clarity.

Figure 2 illustrates the characteristic ΔtrXAS effects of the CuO sample for various pump-probe time delays using the 355 nm, 4.6 mJ/cm² data set as an example. Fig. 2a covers the full spectral range of the measurement, while Fig. 2b provides a magnified view of the first resonance. The static XAS spectrum is overlaid in gray for reference. The left and right ordinates correspond to XAS and ΔtrXAS spectra, respectively. While the XAS units are arbitrary, they are the same for both the XAS and ΔtrXAS spectra. The blue (0.15 ns) and green (2.15 ns) curves correspond to data from the first and second X-ray pulse after excitation, respectively. In order to investigate smaller differences at longer pump-probe delays, where the ΔtrXAS signals are smaller, signals from multiple ALS bunches are averaged for this figure. The red curve (8.15 ns) is an average of three pulses (Δt = 6.15–10.15 ns), the cyan curve (17.15 ns) of six pulses (Δt = 12.15–22.15 ns) and the orange (180.15 ns) of 81 pulses (Δt = 100.15–260.15 ns). For each of the averaged spectra, the indicated delay is the mean delay of the averaged spectra. The by far strongest effects are observed in the region of the first resonance at ~530.1 eV (Cu e_g[30]) which is shown in more detail in Fig. 2b. The difference spectra exhibit a new feature emerging at the low-energy side of the static absorption spectrum (gray) with a peak at ~529.4–529.5 eV. Concurrently, signal is depleted near the static peak maximum with a maximum depletion at ~530.3 eV. The ΔtrXAS spectra exhibit an isosbestic

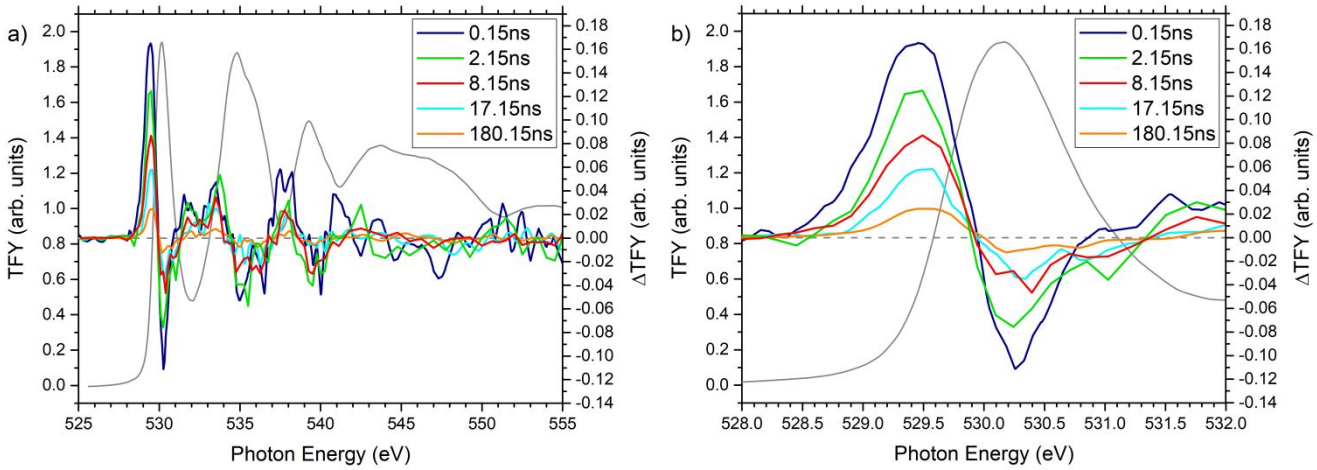

Fig. 2. a) Overview of the 355 nm 4.6 mJ/cm² trXAS data set. The reference spectrum (gray, left ordinate) is shown along with ΔtrXAS spectra at several pump-probe delays (right ordinate). b) The lowest energy resonance at 530.1 eV displays the largest relative changes and is analysed in more detail. See text for details.

point near ~529.9 eV, which separates the signal enhancement and depletion ranges. At first glance, the difference curves resemble differentials of the static XAS spectrum, which would be an indication that they may be described by a simple energy shift (ΔE) of the XAS spectrum upon photoexcitation, i.e. $\Delta trXAS = \alpha \times [trXAS(E-\Delta E) - trXAS(E)]$. However, no combination of parameters α (the fraction of reference spectrum trXAS that is shifted) and ΔE (the shift in X-ray photon energy) can be found that describes the difference spectra reasonably well. This is mostly due to the asymmetry of trXAS signal depletion and emergence, readily apparent in Fig. 2b.

As a first metric to investigate the relaxation dynamics of the photoexcited system, the area underneath the positive peak of the ΔtrXAS spectra in Fig. 2b is plotted as a function of pump-probe delay in Fig. 3. All data sets have been recorded during the same beamtime except for the 355 nm, 2.7 mJ/cm^2 data. In that case, an additional 355 nm, 4.6 mJ/cm^2 scan was performed to ensure it matches the data from the previous experiment and inevitable changes from beamtime to beamtime, such as slight variations of the laser spot size, did not affect the measured signals within the scatter of the data. Each data point in Fig. 3 corresponds to a single pump-probe delay. The amplitudes and dynamic trends of the new low-energy feature vary for different excitation wavelengths and fluences. For the highest fluences (4.6–4.8 mJ/cm^2), however, they are very similar for both 355 nm and 532 nm excitation. Each of these two data sets display a transient behavior marked by two decay timescales of roughly $\tau_1 = 10$ ns and $\tau_2 = 300$ ns. Evidently, the dynamic processes underlying the trXAS signals cannot be characterized by a simple, first-order rate equation. Instead, a more complex description is required that will be derived in section 4 within the framework of a thermal diffusion model.

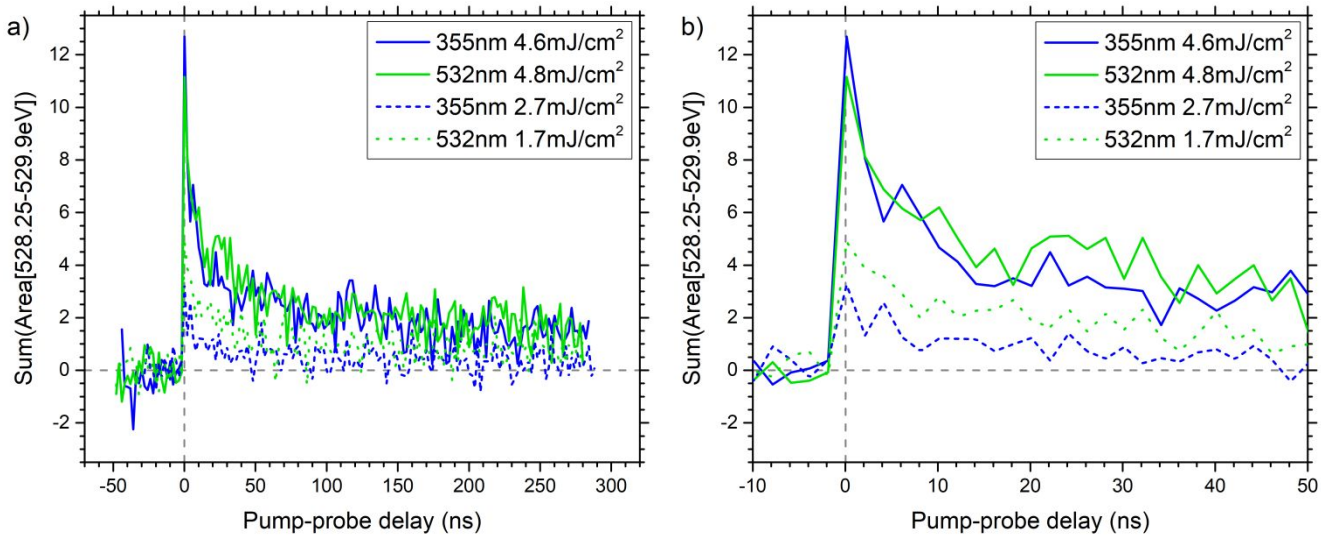

Fig. 3. a) Time-dependent intensity of the positive ΔtrXAS feature, integrated between 528.25 eV and 529.9 eV (Fig. 2b) for all trXAS data sets. b) Magnified view for delays up to 50 ns.

Fig. 4 shows the results of the temperature-dependent XAS_{temp} measurements. Fig. 4a shows the room temperature reference spectrum acquired at 22°C in gray (left ordinate). This reference spectrum is subtracted from spectra acquired at elevated temperatures of 53°C, 77°C, 101°C and 145°C to generate the color coded ΔXAS_{temp} difference spectra as indicated in the figure legend (right ordinate). Fig. 4b shows a magnified view of the region near the Cu e_g resonance.[30] A comparison of Fig. 2 and Fig. 4 reveals striking similarities between the temperature-induced difference spectra $\Delta XAS_{temp}(\Delta T)$ and the photo-induced ΔtrXAS(Δt) data. For every resonance peak of the XAS spectrum (~530 eV, ~535 eV and 539 eV), a signal enhancement feature appears at its low-energy side (529.65 eV, 533.50 eV and 537.75 eV) and a depletion feature at its high-energy side (530.3 eV, 535.5 eV and 539.3 eV). Both the positions and relative heights of these features appear to be very similar in both types of measurements. The second resonance around 535 eV has mainly Cu4s and some Cu3d character[30] and consists of two strongly overlapping peaks. Correspondingly, the ΔXAS_{temp} spectra at higher temperatures exhibit a double peaked depletion feature, likely due to overlapping absorption features. As in the case of the ΔtrXAS data, the most distinct features appear in the spectral range of the Cu e_g resonance. Interestingly, the ΔXAS_{temp} spectra also exhibit an isosbestic point separating the positive and negative difference signal for all measured temperatures. It is located at ~530.0 eV, very close to the ~529.9 eV value for the ΔtrXAS curves.

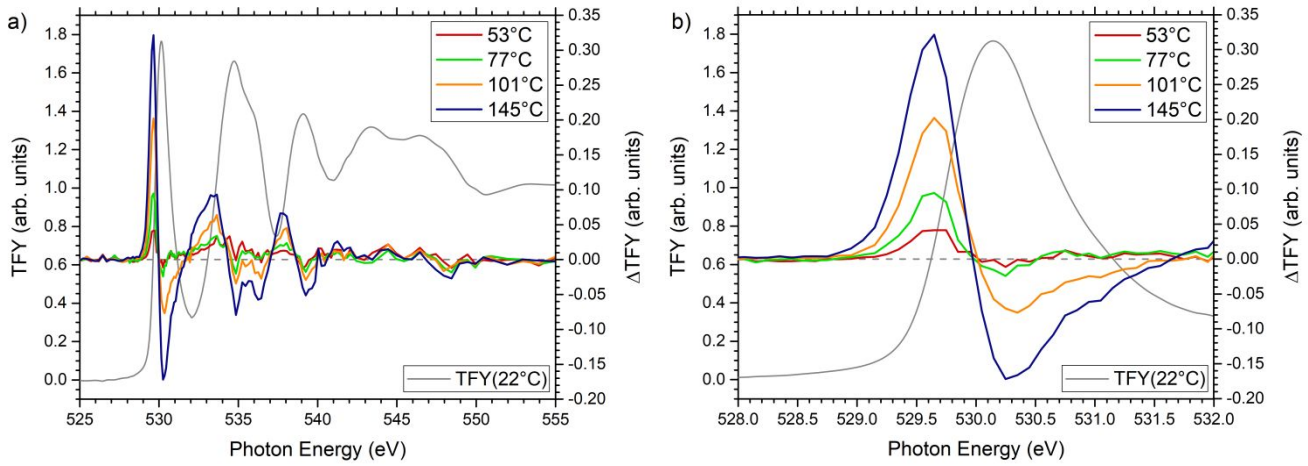

Fig. 4. a) Temperature-dependent difference spectra ΔXAS_{temp} (colored, right ordinate) together with the reference spectrum XAS_{temp}(22°C) measured at room temperature (gray, left ordinate). b) Magnified view near the Cu e_g resonance feature at ~530.1 eV.

4. Data analysis

Different data sets were recorded with slightly different energy resolutions. In particular the XAS_{temp} data (Fig. 4) exhibit better energy resolution than the trXAS data. In order to facilitate a quantitative comparison of all observed difference spectra, the energy resolution mismatch is compensated by identifying the ground state XAS spectrum with the lowest energy resolution (532 nm, 4.8 mJ/cm^2, further on referred to as XAS_{ref}), and convoluting all other data sets with Gaussian functions that effectively impose a common energy resolution on all ground state and RT spectra. Data analysis is restricted to the energy region between 528.25 and 531.75 eV containing the Cu e_g peak at 530.1 eV. This region exhibits the strongest difference features and small differences in the energy scaling across more extended NEXAFS ranges make a quantitative comparison across larger energy ranges challenging. Due to the asymmetric peak shape, the convolution changes the peak position as well. Therefore, for each ground state spectrum, two free fit parameters are used to match it to XAS_{ref}, the FWHM of the Gaussian convolution function and a rigid shift of the entire spectrum. In order to prevent artifacts due to small peak height variations, all spectra are scaled to the same Cu e_g peak height of 1. The FWHM, energy shift and scaling values derived using the ground state spectra are then applied to both the ground and corresponding excited state spectra to calculate the ΔtrXAS and ΔXAS_{temp} difference spectra. Fig. 5a shows the ground state (unpumped) reference spectrum XAS_{ref} (gray, left ordinate) along with ΔtrXAS difference spectra for both excitation wavelengths, 355 nm in blue and 532 nm in green, and two pump laser fluences each at a pump-probe delay of 150 ps (right ordinate). Fig. 5b shows a magnified view of the energy range used for the fit (528.25–531.75 eV). While all data sets show qualitatively

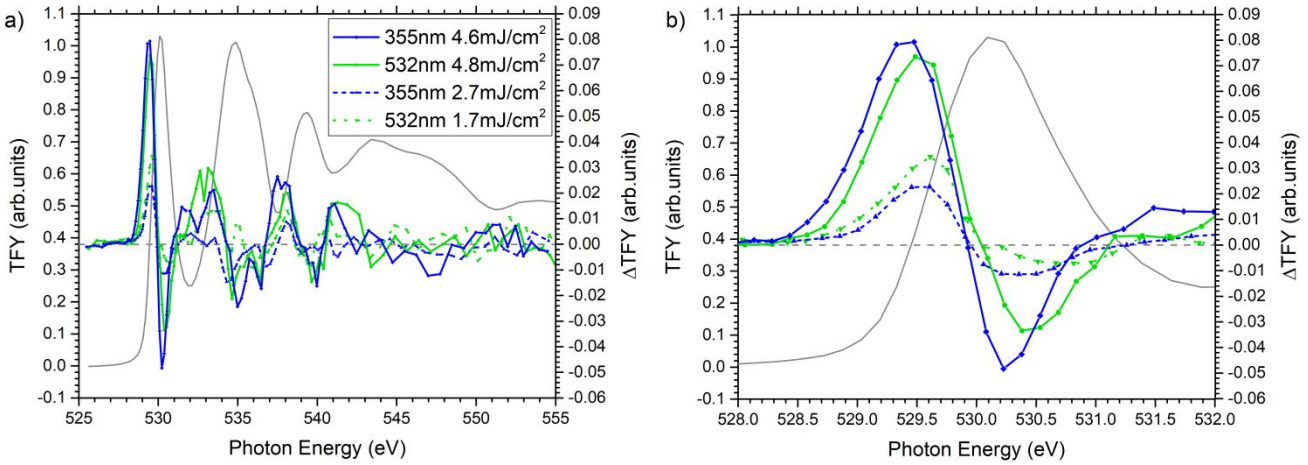

Fig. 5. a) ΔtrXAS difference spectra at a pump-probe delay of 150 ps for both excitation wavelengths and various pump laser fluences. b) Spectral region of the lowest energy feature, Cu e_g, which is used to adjust all data sets toward a common energy resolution. Data is shown after the convolution procedure is applied. The ground state reference spectrum XAS_{ref} is shown in gray in both panels.

similar trends, the best quantitative match is found between the 355 nm, 4.6 mJ/cm^2 and the 532 nm, 4.8 mJ/cm^2 data sets. These comparable difference spectra together with the matching peak areas and similar decay behavior illustrated in Fig. 3 strongly suggest that the observed XAS dynamics are primarily defined by the laser fluence, not the photon energy. In contrast, the excitation density within the probed volume appears to play a less prominent role, as evidenced by the significant differences between the traces associated with the 355 nm, 2.7 mJ/cm^2 and 532 nm, 4.8 mJ/cm^2 data sets shown in Fig. 3 and Fig. 5. In other words, the deposited energy per unit area rather than the number of excitations per unit volume correlates most strongly with the observed transient XAS response, which is a strong indication that thermal effects, rather than the number of excited electrons, generate the dominant contributions to the ΔtrXAS data.

In order to test this hypothesis, a detailed comparison between the two highest fluence ΔtrXAS data (355 nm, 4.6 mJ/cm^2 and 532 nm, 4.8 mJ/cm^2) and the ΔXAS_{temp} data is performed for each pump-probe time delay. The comparison is used to generate time-dependent sample temperature profiles for the two trXAS measurements, which are interpreted with the aid of a thermal diffusion model. As demonstrated below, the model reproduces the non-trivial dynamic trends indicated in Fig. 3 and provides access to time-dependent surface- and bulk-temperatures as well as the thermal conductivity of the sample.

In a first step, a linear interpolation of the XAS_{temp} spectra measured at 22°C, 53°C, 77°C, 101°C and 145°C is performed in 1°C steps in order estimate the shape of the spectra on a finer temperature grid. Spectra for temperature values >145°C are estimated by a corresponding extrapolation using the 101°C and 145°C data. ΔXAS_{temp} spectra similar to Fig. 4 are generated for all interpolated and extrapolated data beyond 28°C by subtracting the (interpolated) reference spectrum at 28°C from the higher temperature spectra. The slightly elevated reference temperature (compared to the nominal 22°C room temperature) is chosen to account for a slight increase in average temperature during the trXAS measurements that is determined with a thermocouple. The 28°C spectrum is also used to determine the convolution parameters described above to match the energy resolution of the temperature-dependent and time-dependent spectra.

Two different fit procedures are applied to derive the time-dependent temperature profiles of the sample volumes probed by the trXAS measurements. The first method is easier to implement, but partly neglects inhomogeneous temperature effects, which are fully included in the second method. In the following, we discuss the results achieved by both methods in order to illustrate which effects need to be taken into account and which approximations are applicable when modeling thermal effects in trXAS spectra of condensed phase samples.

In the first method ("homogeneous fit"), the fit routine determines the temperature T for each time delay Δt, for which the absolute difference between the $\Delta XAS_{temp}(T)$ and the $\Delta trXAS(\Delta t)$ spectra (integrated over the energy range of the Cu e_g resonance) is minimal. Fig. 6a shows the result of this fit procedure for the 532 nm, 4.8 mJ/cm^2 data set at a pump-probe delay of 150 ps. Depicted are the ΔtrXAS(150 ps) spectrum (green) and the best fit (red) corresponding to the curve $\Delta XAS_{temp}(73°C) = XAS_{temp}(101°C) - XAS_{temp}(28°C)$. The residual of the fit is shown as a dashed, black curve. Fig. 6b illustrates the convergence of the fit. The black trace is derived by integrating the absolute value of the residual across the fit energy range for each interpolated $\Delta XAS_{temp}(T)$ spectrum. The minimum position corresponds to the best fit shown in Fig. 6a.

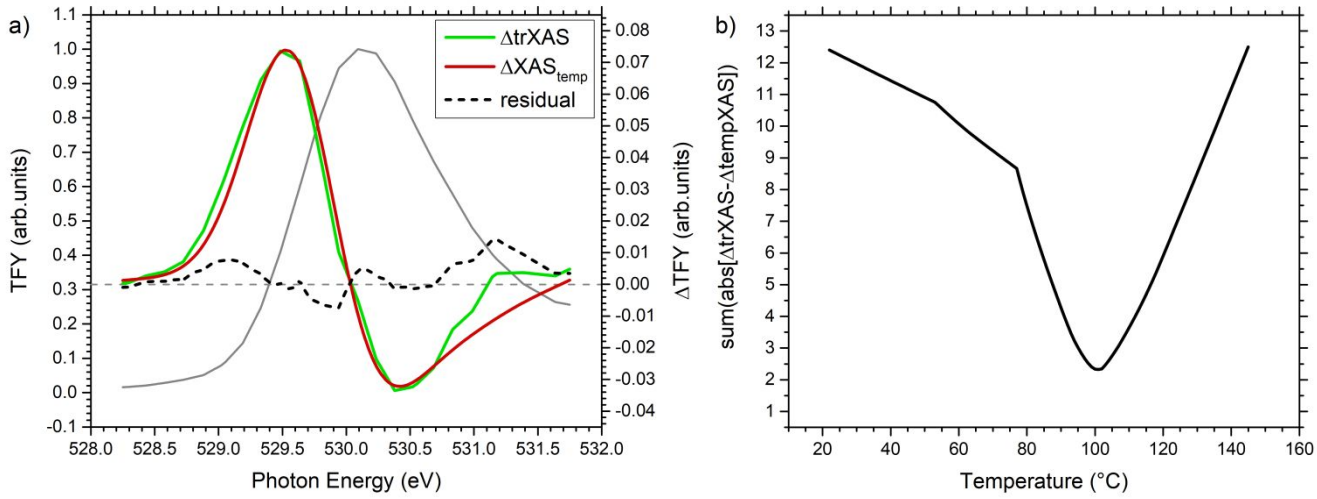

Fig. 6. a) Photoinduced oxygen K-edge trXAS difference spectrum (ΔtrXAS, green) upon excitation of CuO with 532 nm, ~5 mJ/cm^2 pulses, probed after 150 ps. The best fit by a temperature-dependent difference spectrum (ΔXAS_{temp}) is shown in red, the fit residual in black (dashed). For reference, the ground state XAS spectrum is shown in gray. All difference spectra refer to the right ordinate, the ground state spectrum to the left ordinate. b) Integral over the absolute value of the fit residual curve in a) as a function of temperature. The fit routine chooses the minimum of this curve to determine the best ΔXAS_{temp} fit to the ΔtrXAS data.

The best fit quality varies for different time delays and the corresponding residual curve (as shown in Fig. 6b) is flatter for longer time delays. Nevertheless, the fit always converges to a single temperature to best reproduce the measured ΔtrXAS(Δ*t*) spectrum. Note that the temperature *T* is the only free parameter of the fit in this method. Note that for any fixed values of *T* and Δ*t*, the amplitudes of the $\Delta XAS_{temp}(T)$ and ΔtrXAS(Δ*t*) spectra are determined by normalizing the Cu e_g peak heights of the XAS_{temp}(28°C) and the ground state trXAS spectra to 1.

Performing this fit for all pump-probe time-delays leads to the time-dependent temperature estimates displayed in Fig. 7. Fig. 7a shows the results for the 355 nm, 4.6 mJ/cm² data (blue diamonds), Fig. 7b the corresponding results for the 532 nm, 4.8 mJ/cm² data (green circles). Similar to the traces shown in Fig. 3, the dynamic trends are marked by a fast initial decay within 10's of nanoseconds, followed by a much slower relaxation on 100's of nanosecond timescales. The data are interpreted with the aid of a thermal diffusion model represented by the solid curves in Fig. 7.

The model is based on the assumption that a certain amount of thermal energy is deposited by the pump pulse within a near-surface volume and then propagates further into the bulk by thermal diffusion. Heat transport by convection is neglected, since the experiment is conducted at a pressure <5×10^{-9} mbar. A simple estimate shows that radiative heat loss is negligible, too. According to the Stefan-Boltzmann law, the total radiated power of a black body at 120°C is ~1.4 kW/m². Using a FWHM laser beam size of roughly 250×250 µm² and a pulse energy of 3 µJ, the fraction of pulse energy emitted within the first 300 ns is 7×10^{-6}, which is negligible within the precision of the experiment. Even when allowing for substantially higher temperatures within the first 150 ps before the first probe pulse arrives, the order of magnitude of this estimate would be unaffected. Heat conduction is modeled as a one-dimensional diffusion process along the surface normal, *z*. For CuO, the optical penetration depths of 21 nm (λ=355 nm) and 125 nm (λ=532 nm)[32,33] as well as the effective X-ray probing depth of 43 nm[34] (see section 2.3) are three to four orders of magnitude smaller than the FWHM of the laser spot (150–250 µm). Furthermore, the diameter of the area probed by the X-ray beam is only about half of the laser spot size. Therefore, the excited and probed sample volumes can be thought of as thin, concentric disks. The characteristic temperature gradients in and around the probed sample volume are thus orders of magnitude larger along the surface normal compared to radial directions parallel to the surface. Consequently, heat transport within the sample may be modeled by diffusion along an insulated cylinder with no lateral heat loss as described by[35,36,37]

$$\frac{\delta Q}{\delta t} = -k * A \frac{\delta T(t,z)}{\delta z}. \quad (1)$$

Here, δ*Q* is the amount of thermal energy transferred through a cross-sectional area *A* per time δ*t*, *k* is the thermal conductivity and *T* is the temperature profile as a function of time *t* and depth *z* relative to the sample surface. The thermal conductivity is assumed to be constant for simplicity and because slight temperature dependencies would be negligible compared to the overall precision of the analysis presented here. The temperature distribution at time zero *T*(*t*=0,*z*) is proportional to the derivative of the depth-dependent laser intensity $I_{laser}(z) = \exp[-z/\delta_{laser}(\lambda)]$, where δ_{laser} is the laser penetration depth. The amplitude of the resulting exponential function is the initial temperature increase after laser

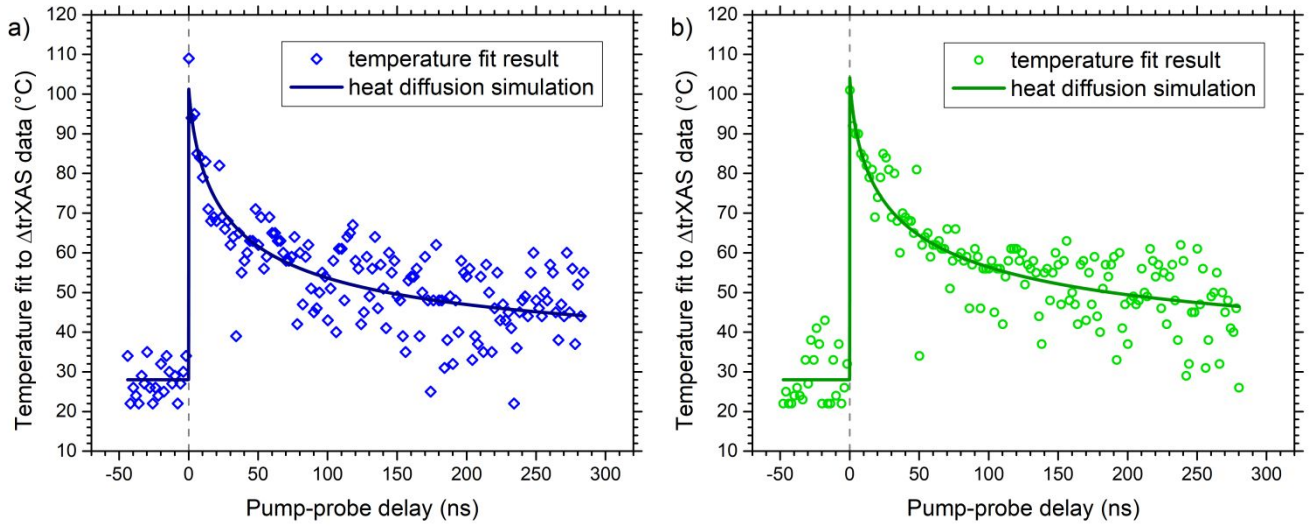

Fig. 7. Time-dependent sample temperatures for excitation with a) 355 nm (blue diamonds) and b) 532 nm (green circles) pulses at fluences of ~5 mJ/cm². Temperatures are derived by a homogeneous temperature fit model that determines a single effective temperature for the probed sample volume. The solid curves are fit results, describing the data within a one-dimensional thermal diffusion model. See text for details.

excitation at the surface $\Delta T(t=0,z=0)$. This boundary condition leads to

$$T(t=0,z) = \frac{(1-R(\lambda))\cdot E_{pulse}}{2\cdot\rho\cdot A\cdot c(T)\cdot\delta(\lambda)_{laser}}\cdot e^{-\frac{z}{\delta(\lambda)_{laser}}} + T_{ref}\,, \quad (2)$$

where $R(\lambda)$ is the sample reflectivity, E_{pulse} is the laser pulse energy, $\delta_{laser}(\lambda)$ the 1/e laser penetration depth, ρ the sample density, A is the FWHM laser spot size and $c(T)$ the specific heat capacity.[38] The sample equilibrium temperature T_{ref} = 28°C is added to the laser induced temperature jump to convert to an absolute temperature scale $T(t=0,z)$. Using eqn. (2) and the experimental parameters given above, the initial surface temperature estimates are $T(0,0)$ = 747°C for 355 nm (4.6 mJ/cm²) and $T(0,0)$ = 157°C for 532 nm (4.8 mJ/cm²) excitation, respectively.

The subsequent thermal diffusion process is modeled numerically by an iterative computer simulation. Based on an initial temperature profile $T(t=0,z)$ according to eqn. (2), it calculates the amount of heat dQ transferred to and from each volume element $A*dz$ within a short time step dt using eqn. (1). The slightly modified thermal energy distribution is used to calculate a new temperature profile $T(t+dt,z)$, which in turn is employed to calculate the depth-dependent heat transfer rates during the next time step and so on. Typical time and depth step sizes are dt = 10 ps and dz = 3 nm, respectively. Convergence of the simulation is tested by varying these step sizes and ensuring that the results are not affected within the overall precision of the method.

For the first, basic temperature analysis presented in Fig. 7, the effective temperature $T_{eff}(t)$ probed by the X-ray pulse is estimated by multiplying the simulated temperature profile $T(t,z)$ with the probe intensity distribution $I_{X\text{-}rays}(z) \sim exp[-z/\delta_{X\text{-}rays}]$ and integrating the result over z. Here, $\delta_{X\text{-}rays}$ is the effective 1/e X-ray escape depth described in section 2.3. The free parameters varied during the fit are the amplitude of the initial temperature distribution $T(t=0,z=0)$, i.e., the initial surface temperature, and the thermal conductivity k. The best fit results, shown as solid curves in Fig. 7, correspond to thermal conductivities of $k_{355\text{ nm}}$ = (0.16±0.06) W m^{-1} K^{-1}, $k_{532\text{ nm}}$ = (1.3±0.5) W m^{-1} K^{-1} and initial surface temperatures of $T(0,0)_{355\text{ nm}}$ = (190±20)°C, $T(0,0)_{532\text{ nm}}$ = (120±11)°C. While a substantial difference in the initial surface temperatures is to be expected for the two laser colors due to the factor of ~6 difference in absorption depths, the thermal conductivities should ideally be the same within the precision of the method. In order to improve the temperature dynamics estimates and to get a better understanding of factors affecting the precision of the fit results, a second more advanced temperature modeling and dynamics fit procedure is applied ("inhomogeneous fit").

A key challenge is that each of the XAS_{temp} spectra is acquired at a single temperature that is constant throughout the entire sample, while temperatures in the trXAS experiments vary significantly within the probed sample volume. The first, homogeneous fit method described above hinges on the assumption that an effective temperature T_{eff} can be defined for the probed volume by a weighted average of an extended temperature profile and that the measured $\Delta trXAS(t)$ spectrum emerging from this volume is well represented by the corresponding $\Delta XAS_{temp}(T_{eff})$ spectrum measured with a homogeneous temperature T_{eff} across the entire sample. However, the temperature dependence of the ΔXAS_{temp} spectra is nontrivial (see Fig. 4) and, generally, the (weighted) average spectrum $\Delta XAS_{temp}^{avg} = \sum_i w_i \Delta XAS_{temp}(T_i) / \sum_j w_j$ of the probed sample volume does not have to be well approximated by the corresponding difference spectrum $\Delta XAS_{temp}(T_{eff})$ measured at the average temperature $T_{eff} = \sum_i w_i(T_i) / \sum_j w_j$. The quality of the approximation is expected to depend strongly on the range of temperatures within the probed volume. For the 532 nm data, the optical penetration depth of 125 nm is significantly larger than the X-ray probing depth of 43 nm, leading to a relatively homogeneous temperature distribution within the probed sample volume and the approximation is expected to hold fairly well. In contrast, for 355 nm excitation, the penetration depth is only 21 nm, much smaller than the X-ray probing depth, resulting in a strongly inhomogeneous temperature distribution within the probed volume, at least for short pump-probe delays. In this case, the approximation is expected to break down.

In order to avoid potential shortcomings of the effective homogeneous temperature approach, a modified inhomogeneous fit procedure is applied that explicitly takes into account both the time- and depth-dependent temperature profiles as well as the complex correlation between local temperatures and corresponding ΔXAS_{temp} profiles. Starting with a thermal conductivity value k and an initial surface temperature $T(0,0)$, the 2D matrix $T(t,z)$ of a time- and depth-dependent temperature profile is calculated using the numerical model based on eqn. (1). This provides, in particular, a temperature distribution $T_N(z)$ at the time of arrival of each probe pulse N, i.e., $T_N(z)=T(t_N=t(bunch\ N), z)$. The simulated spectrum $\Delta trXAS_{sim}(E, t_N)$ for each bunch N is then calculated as the weighted average of the $\Delta XAS_{temp}(E, T_N(z))$ spectra using the X-ray intensity distribution $I_{X\text{-}rays}(z) \sim exp[-z/\delta_{X\text{-}rays}]$ as the weight function:

$$\Delta trXAS_{sim}(E,t_N) = \frac{\sum_z I_{X-rays}(z)\ \cdot\ \Delta XAS_{temp}(E,T_N(z))}{\sum_{z'} I_{X-rays}(z')}. \quad (3)$$

During the fit procedure, the values of k and $T(0,0)$ are varied such that the sum of *all* residuals $R_{total} = \sum_N R_N = \sum_N \sum_E |\Delta\text{trXAS}_{sim}(E,t_N) - \Delta\text{trXAS}(E,t_N)|$ for all energies E within the range 528.25 - 531.75 eV and for all times t_N is minimized. This inhomogeneous fit procedure leads to best fit values of $k_{355\text{ nm}} = 0.29\ ^{+0.11}_{-0.07}$ W m^{-1} K^{-1}, $k_{532\text{ nm}}$ = (1.3±0.4) W m^{-1} K^{-1} for the heat conductivities and $T(0,0)_{355\text{ nm}}$ = (230±30)°C, $T(0,0)_{532\text{ nm}}$ = (123±10)°C for the initial surface temperatures at the two excitation wavelengths. Uncertainties correspond to one sigma standard deviations computed from the fit residuals according to eqn. (12) in ref. [39]. As expected, the values for 532 nm are very similar to the

results derived with the homogeneous, effective temperature fit model, while the values for 355 nm differ considerably.

differ notably from each other for the 355 nm data set (Fig. 8a). The large differences in the fit results for the 355 nm and 532 nm data are rooted in the different absorption depths of the two excitation

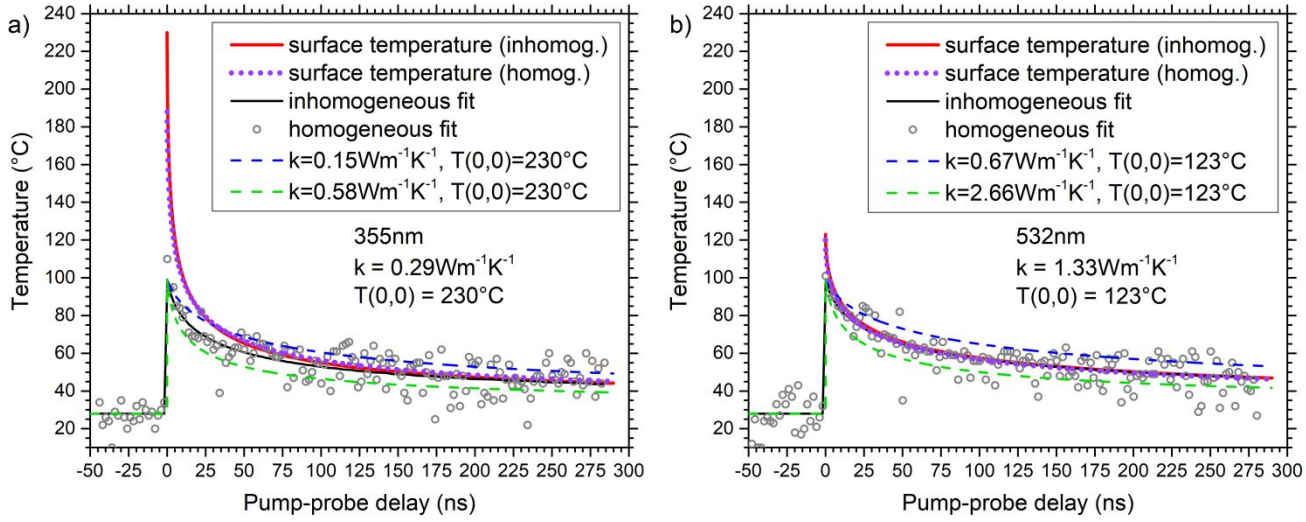

Fig. 8. Temperature dynamics resulting from the two fit models as a function of pump-probe delay for excitation with a) 355 nm and b) 532 nm. Singular data points (gray) are the result of the effective, homogeneous temperature model, the black line the result of the inhomogeneous fit model. Red and violet (dotted) lines show the surface temperature dynamics derived from the inhomogeneous and homogeneous fit models, respectively. Blue and green dashed lines indicate the variation of the inhomogeneous fit model results when varying the heat conductance by factors of 1/2 and 2, respectively, compared to the best fit values, while keeping the surface temperature constant.

Figure 8 shows a comparison of the results from the two modeling procedures for both excitation wavelengths. Gray circles are the result of the homogeneous, single effective temperature fits (same as data points in Fig. 7) while the black solid lines result from the inhomogeneous fit routine. Similar to the homogeneous fit curves in Fig. 7, the inhomogeneous fit curves in Fig. 8 are generated by multiplying the simulated temperature profiles $T(t,z)$ with the probe intensity distribution $I_{X\text{-}rays}(z) \sim exp[-z/\delta_{X\text{-}rays}]$ and integrating the results over z. In order to illustrate the effect of varying the thermal conductivity parameter k in the inhomogeneous fit routine, two dashed lines are added, corresponding to the temperature transients computed with half (blue) and double (green) the best fit value of k, while keeping the surface temperatures $T(0,0)$ constant. The curves indicate a pronounced sensitivity of the temperature trends to the absolute value of the thermal conductivity.

Note that the homogeneous and inhomogeneous fit procedures lead to almost identical volume-averaged temperature trends (solid curves in Fig. 7, black curves in Fig. 8). The best fit values for k and $T(0,0)$, however, agree for both fit procedures only for 532 nm excitation, while they differ significantly for the 355 nm data. For the latter, the reconstructed surface temperatures also differ from the volume-averaged ones while they agree reasonably well for the 532 nm measurement. This is illustrated by the red and violet (dotted) curves in Fig. 8, which show the surface temperature trends, $T(t,0)$, for the inhomogeneous and homogeneous fits, respectively. For 532 nm, the two surface temperature curves and the black curve are very similar (Fig. 8b). In contrast, all three curves

wavelengths in relation to the X-ray escape depth. This is illustrated in more detail in Fig. 9, which shows the temperature distributions at time zero (gray lines) and for the first nine probe pulses (colored lines) after excitation, reconstructed with the inhomogeneous fit model. Fig. 9a and 9b show the results for 355 nm and 532 nm excitation, respectively. For comparison, the X-ray escape profile, offset by the sample equilibrium temperature and scaled to the initial surface temperature, is overlaid as a solid black line in both panels. Note the different ranges of z-values in Fig. 9a and 9b. As expected from the different optical penetration depths, the temperature profiles have much higher gradients and spread across a larger range of values for the 355 nm compared to the 532 nm experiment. These details, however, are largely obscured in the volume-averaged temperatures "seen" in the experiment. Thus, the striking similarities between the observed volume-averaged temperature dynamics for 355 nm and 532 nm excitation displayed in Fig. 7 and Fig. 8 conceal significant differences in the underlying physical phenomena that need to be recovered through careful analysis and modeling. We note that the appearance of significantly higher surface temperatures in the 355 nm compared to the 532 nm experiment is independently corroborated by a more efficient conversion of CuO to Cu_2O upon UV excitation of the sample compared to the visible excitation. This leads to the emergence of an additional signal in the CuO XAS spectrum at the location of the ~532 eV white line of the Cu_2O spectrum (see Fig. 1a), which needs to be suppressed by scanning every sample spot only once in the 355 nm experiment. Thus, the striking similarities between the observed temperature dynamics for 355 nm and 532 nm excitation

displayed in Fig. 7 and Fig. 8 conceal significant differences in the underlying physical phenomena that need to be recovered through careful analysis and modeling of the depth-dependent optical excitation and X-ray probing profiles.

dominant effects in the ΔtrXAS spectrum are indeed due to thermal effects with contributions from both thermal disorder and lattice distortions.[7]

The study presented here reproduces a predominance of lattice

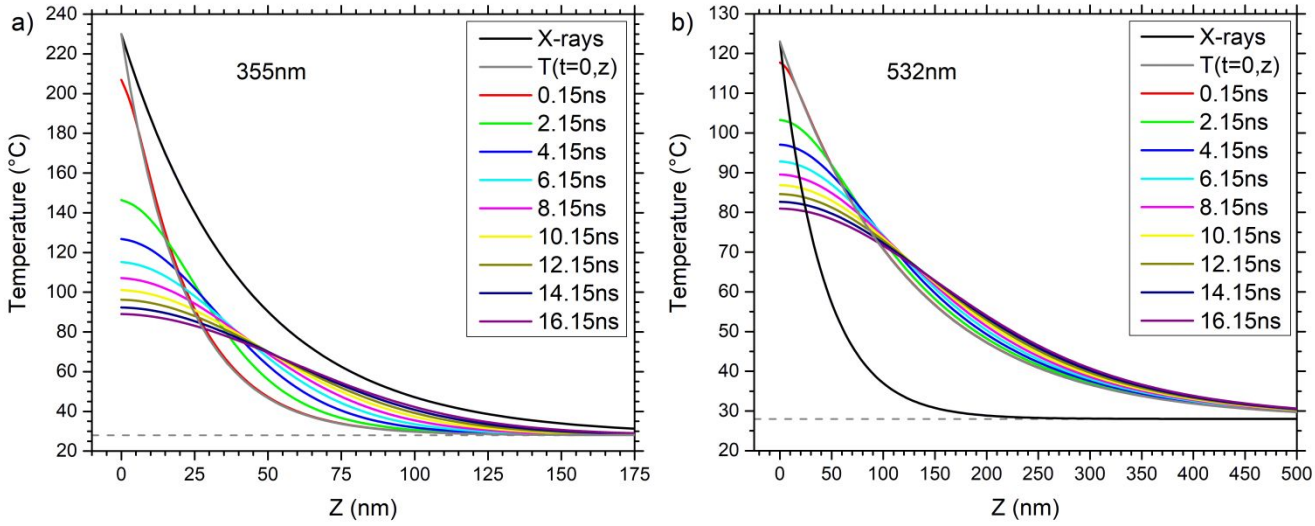

Fig. 9. Time-dependent temperature distributions for a) 355 nm and b) 532 nm excitation as a function of distance *z* from the surface along the surface normal. The gray line corresponds to $t \approx 0$ and colored lines to the times of arrival of the first nine X-ray pulses following the laser excitation. For reference, the depth-dependent X-ray probe intensity, offset by the sample equilibrium temperature and scaled to the initial surface temperature, is shown in black.

5. Discussion

The results presented above strongly suggest that the photoinduced changes in the XAS spectra of CuO beyond ~100 ps pump-probe delay are dominated by thermal effects. This observation is in agreement with the results of Hayes et al.[7] and Lin et al.[8] for super-bandgap excited α-Fe_2O_3 and PbI_2, respectively. Lin et al. excited ~70 nm thick polycrystalline films of PbI_2 (deposited on 50 nm thick silicon nitride) with 400 nm radiation and probed the induced dynamics with femtosecond time-resolved XUV absorption at the iodine 4d level near ~50 eV.[8] Good agreement was found between the photoinduced XUV absorption change after 40–100 ps and a temperature-dependent absorption change induced by heating the sample from 20°C to 120°C. A complementary ultrafast electron diffraction experiment by the same group corroborated the finding that temperature effects start to dominate the pump-probe difference spectra after ~4 ps.[8] Hayes et al. performed oxygen and iron K-edge trXAS measurements on 20 nm thick films of hematite (α-Fe_2O_3, deposited on 100 nm thick silicon nitride) excited with 400 nm and 351 nm pulses, respectively.[7] The Fe K-edge ΔtrXAS spectrum at 100 ps pump-probe delay is well reproduced by a ΔXAS_{temp} spectrum generated by subtracting a steady-state XAS spectrum recorded at ~30°C from one acquired at ~230°C. Corresponding theoretical modeling of the spectra using multiple scattering calculations confirmed that the temperature induced effects in picosecond trXAS for another transition metal oxide semiconductor. In addition, it provides further insight into the temporal evolution of lattice temperature profiles after laser excitation on an absolute temperature scale with a temporal sensitivity and a spatial selectivity on the order of 10's of picoseconds and 10's of nanometers, respectively. The results presented in Fig. 7 and Fig. 8 indicate that the heat transport dynamics may be approximated by a one-dimensional diffusion model as previously employed in picosecond time-resolved electron diffraction studies of laser-heated metal surfaces.[35] However, comparison of the trXAS results for 355 nm and 532 nm excitation also reveals that a quantitative interpretation of the underlying physics requires detailed understanding and modeling of the relation between the temperature distribution within the sample and the resulting X-ray spectroscopic signatures. In order to understand and predict thermal effects in time-dependent X-ray absorption spectra, it should be ensured that the X-ray probing depth is small compared to the penetration depth of the optical excitation. Otherwise, signal contributions from regions with significantly different temperatures need to be disentangled. This effect is documented by the significant fit-model dependence of both the reconstructed temperature profiles as well as the thermal conductivity *k* in the 355 nm experiment. In contrast, the corresponding results for the 532 nm measurements are largely model-independent.

Additional evidence that the 532 nm experiment is better understood on a quantitative level is provided by a comparison of

the fit results with surface temperature predictions based on eqn. (2). The calculated surface temperature after absorption of a 532 nm pump pulse with a fluence of 4.8 mJ/cm^2 is $T(0,0)_{532nm}$(calc) = 157°C, which agrees reasonably well with the outcome of the inhomogeneous fit $T(0,0)_{532nm}$(fit) = 123°C. In contrast, the corresponding values for 355 nm excitation are $T(0,0)_{355nm}$(calc) = 747°C, $T(0,0)_{355nm}$(fit) = 230°C, i.e., the calculated and reconstructed temperature jumps differ by a factor of ~3.6. The reason for this large discrepancy is currently unknown. One contributing factor may be that, despite our best efforts, the convolution methods described in section 4 could provide an inaccurate modeling of the ΔtrXAS response if the sampled region exhibits a steep-gradient temperature distribution. Another potential issue is that the ΔXAS_{temp} spectra for temperatures above 145°C have been estimated based on a linear extrapolation of the measurements at 101°C and 145°C, which is most likely increasingly inaccurate with increasing temperatures. Interestingly, Hayes et al. also observed a significant discrepancy between the estimated temperature rise in their hematite sample based on the absorbed photon energy (~470°C) and the steady-state temperature rise needed to reproduce the photon-induced change in X-ray absorption (200°C).[7] In this case, temperature gradients should not play a major role due to the small sample thickness of only 20 nm. Note that in both cases, the hematite experiment using 351 nm excitation and the CuO experiment at 355 nm excitation, the temperature rise estimated by a complete conversion of the absorbed laser pulse energy into heat is much larger than the measured temperature increase based on a comparison to steady-state temperature-dependent ΔXAS_{temp} spectra. Additionally, the estimated temperatures in both cases were significantly higher than the highest temperatures during the steady-state measurements used to determine the ΔXAS_{temp} response. Thus, it could be that this response saturates toward higher temperatures, which would limit their impact on the XAS fingerprint. Further studies with higher reference temperatures are required to gain a better understanding of this regime.

Given the challenges associated with the quantitative analysis of the 355 nm experiment, we restrict a more detailed discussion of the fit results to the 532 nm measurement. The good agreement between the observed and reconstructed temperature dynamics illustrated in Fig. 7b, between the absolute temperature values derived from the absorbed laser pulse energy and the dynamics fit, as well as the model-independence of the fit results for 532 nm excitation suggest that heat transport within the CuO sample is well represented by a thermal diffusion constant k = (1.3±0.4) W m^{-1} K^{-1}. Literature values for the thermal conductivity of CuO vary across almost two orders of magnitude from 1.013 W m^{-1} K^{-1} in ref. 24 to 18 W m^{-1} K^{-1} in ref. 25, 33 W m^{-1} K^{-1} in ref. 40 and 78 W m^{-1} K^{-1} in ref. 41. We note, however, that an extensive literature search did not yield any original reference that would describe the experiments used to derive any of these values. Thus, it is not entirely clear whether the large variance is primarily the result of different sample preparation techniques or of uncertainties in the measurements. Notably, however, the smallest value, reported by Samsonov[24] is the only one for which the sample form is indicated as powder. Given that this value is remarkably close to the one derived here and that all other literature values are more than an order of magnitude larger, it appears that the thermal conductivity of the CuO film prepared in this study most closely resembles that of a CuO powder.

At first glance, this result may be surprising as the sample is prepared by annealing a solid sheet of copper. Note, however, that the CuO sample consists of a relatively thin film at the Cu surface and the oxidation process is likely accompanied by significant changes in the surface morphology. Gong et al. used annealed sputtering to deposit thin films of copper at temperatures between 200°C and 400°C in air and studied the resulting surfaces using X-ray diffraction (XRD), Raman spectroscopy, and atomic force microscopy (AFM).[26] It was concluded that, below 300°C, Cu is oxidized to Cu_2O and, upon further temperature increase ≥300°C, CuO is formed. In particular, the AFM images reveal substantial surface morphology variations during the phase transitions. During the Cu_2O formation, the surface roughness increases from ~10's to ~100's of nanometer while grains of Cu_2O form and coalesce to typical grain sizes of ~150 nm. At 400°C, CuO forms in lamellar secondary grains with a thickness of ~5 nm, which are distributed within the larger Cu_2O grains. Based on these observations, it is conceivable that the CuO film prepared here by heating of a Cu surface in air to 500°C is also marked by a nano-structured morphology rather than a crystalline bulk structure. In this case, the thermal conductivity of the film may be expected to lie closer to the value for a CuO powder than a crystalline bulk sample. Further characterization of the CuO film using alternative techniques may provide additional insight in this regard.

6. Conclusion and outlook

Photoinduced changes in the oxygen K-edge X-ray absorption spectrum of a thin film of CuO have been studied by picosecond time-resolved XAS and complementary steady-state temperature-dependent XAS. The results show that for pump-probe delays ≥150 ps, the trXAS spectra are dominated by lattice temperature induced effects for both 355 nm and 532 nm excitation. The laser-induced heating and subsequent sample cooling dynamics at pump laser fluences of ~5 mJ/cm^2 are well described by a one-dimensional thermal diffusion model that explicitly takes into account the depth-dependence of both the optical excitation and the X-ray probing. A comparison of the measurements with different pump laser wavelengths shows that a detailed modeling of these depth-dependent profiles is crucial for a quantitative understanding of the thermal dynamics in terms of the material properties. Vice-versa, predicting the impact of thermal excitations on future trXAS studies will require a correspondingly well-developed understanding of the sample properties and nanoscale

intensity profiles of pump- and probe-pulse intensities. The thermal conductivity of the CuO sample used in this study, $k = (1.3\pm0.4)$ W m^{-1} K^{-1}, is in good agreement with the literature value for CuO powder, $k_{powder} = 1.013$ W m^{-1} K^{-1},[24] and approximately an order of magnitude smaller than the smallest literature value for bulk CuO, $k_{bulk} = 18$ W m^{-1} K^{-1}.[25] This underlines the importance of proper sample characterization prior to a trXAS experiment. A prediction of, for example, how fast thermal excitations in the CuO film may be removed between pump-pulses of a high repetition-rate trXAS experiment would lead to a far too optimistic estimate if it were based on the bulk properties of cupric oxide. Moreover, a predictive understanding of thermal dynamics and their spectral fingerprints is not only important to mitigate sample damage and unwanted signal contributions but also to perform experiments where photoinduced thermal excitations are the actual trigger for the dynamics under investigation.[5] The results presented here demonstrate that a quantitative modeling of thermal effects in trXAS spectra is possible but also that it requires great dedication to detail regarding the material properties and experimental conditions of the pump-probe experiment to make quantitatively accurate predictions.

7. Conflicts of interest

There are no conflicts to declare.

8. Acknowledgments

This work was supported by the U.S. Department of Energy, Office of Science, Office of Basic Energy Sciences, Chemical Sciences, Geosciences and Biosciences Division, through Contract No. DE-AC02-05CH11231. This research used resources of the Advanced Light Source, which is a DOE Office of Science User Facility under contract no. DE-AC02-05CH11231. J.M. acknowledges partial support from the ALS Doctoral Fellowship in Residence Program (2017). SN and MB acknowledge support by the Alexander von Humboldt foundation. F.R. acknowledges financial support by VI 419 of the Helmholtz Association. FR and WE were supported by the Helmholtz Research Association (Germany) within the framework program of 'structure of matter'. WE also would like to acknowledge the hospitality of the ALS during some extended visits.

9. References

1 M. L. Grünbein, J. Bielecki, A. Gorel, M. Stricker, R. Bean, M. Cammarata, K. Dörner, L. Fröhlich, E. Hartmann, S. Hauf, M. Hilpert, Y. Kim, M. Kloos, R. Letrun, M. Messerschmidt, G. Mills, G. Nass Kovacs, M. Ramilli, C. M. Roome, T. Sato, M. Scholz, M. Sliwa, J. Sztuk-Dambietz, M. Weik, B. Weinhausen, N. Al-Qudami, D. Boukhelef, S. Brockhauser, W. Ehsan, M. Emons, S. Esenov, H. Fangohr, A. Kaukher, T. Kluyver, M. Lederer, L. Maia, M. Manetti, T. Michelat, A. Münnich, F. Pallas, G. Palmer, G. Previtali, N. Raab, A. Silenzi, J. Szuba, S. Venkatesan, K. Wrona, J. Zhu, R. B. Doak, R. L. Shoeman, L. Foucar, J.-P. Colletier, A. P. Mancuso, T. R. M. Barends, C. A. Stan and I. Schlichting, *Nature Communications*, 2018, **9**, 3487.

2 R. W. Schoenlein et al., LCLS-II Science Opportunities, Report SLAC-R-1053 (SLAC National Accelerator Laboratory, Menlo Park CA), https://portal.slac.stanford.edu/sites/lcls_public/Lists/Publications/DispForm.aspx?ID=1004&ContentTypeId=0x0100D2D2C16F06384A44A845B10E6FC226F600DC7CB9184F2FB34484887A99919A7390, (accessed 1 December 2018).

3 S. M. Teichmann, F. Silva, S. L. Cousin, M. Hemmer and J. Biegert, *Nature Communications*, 2016, **7**, 11493.

4 D. Popmintchev, B. R. Galloway, M.-C. Chen, F. Dollar, C. A. Mancuso, A. Hankla, L. Miaja-Avila, G. O'Neil, J. M. Shaw, G. Fan, S. Ališauskas, G. Andriukaitis, T. Balčiunas, O. D. Mücke, A. Pugzlys, A. Baltuška, H. C. Kapteyn, T. Popmintchev and M. M. Murnane, *Physical Review Letters*, 2018, **120**, 093002.

5 H. Öström, H. Öberg, H. Xin, J. LaRue, M. Beye, M. Dell, J. Gladh, M. L. Ng, J. A. Sellberg, S. Kaya, G. Mercurio, D. Nordlund, M. Hantschmann, F. Hieke, D. Kühn, W. F. Schlotter, G. L. Dakovski, J. J. Turner, M. P. Minitti, A. Mitra, S. P. Moeller, A. Föhlisch, M. Wolf, W. Wurth, M. Persson, J. K. Nørskov, F. Abild-Pedersen, H. Ogasawara, L. G. M. Pettersson and A. Nilsson, *Science*, 2015, **347**, 978–982.

6 M. Schultze, K. Ramasesha, C. D. Pemmaraju, S. A. Sato, D. Whitmore, A. Gandman, J. S. Prell, L. J. Borja, D. Prendergast, K. Yabana, D. M. Neumark and S. R. Leone, *Science*, 2014, **346**, 1348–1352.

7 D. Hayes, R. G. Hadt, J. D. Emery, A. A. Cordones, A. B. F. Martinson, M. L. Shelby, K. A. Fransted, P. D. Dahlberg, J. Hong, X. Zhang, Q. Kong, R. W. Schoenlein and L. X. Chen, *Energy & Environmental Science*, 2016, **9**, 3754–3769.

8 M.-F. Lin, M. A. Verkamp, J. Leveillee, E. S. Ryland, K. Benke, K. Zhang, C. Weninger, X. Shen, R. Li, D. Fritz, U. Bergmann, X. Wang, A. Schleife and J. Vura-Weis, *The Journal of Physical Chemistry C*, 2017, **121**, 27886–27893.

9 S. Harish, J. Archana, M. Sabarinathan, M. Navaneethan, K. D. Nisha, S. Ponnusamy, C. Muthamizhchelvan, H. Ikeda, D. K. Aswal and Y. Hayakawa, *Applied Surface Science*, 2017, **418**, 103–112.

10 R. Saravanan, S. Karthikeyan, V. K. Gupta, G. Sekaran, V. Narayanan and A. Stephen, *Materials Science and Engineering: C*, 2013, **33**, 91–98.

11 S. Xu, A. J. Du, J. Liu, J. Ng and D. D. Sun, *International Journal of Hydrogen Energy*, 2011, **36**, 6560–6568.

12 J. Yu, Y. Hai and M. Jaroniec, *Journal of Colloid and Interface Science*, 2011, **357**, 223–228.

13 J. Bandara, C. P. K. Udawatta and C. S. K. Rajapakse, *Photochemical & Photobiological Sciences*, 2005, **4**, 857.

14 W. Zhang, G. Ma, H. Gu, Z. Yang and H. Cheng, *Journal of Power Sources*, 2015, **273**, 561–565.

15 S. Neppl, J. Mahl, A. S. Tremsin, B. Rude, R. Qiao, W. Yang, J. Guo and O. Gessner, *Faraday Discussions*, 2016, **194**, 659–682.

16 N. Serin, T. Serin, Ş. Horzum and Y. Çelik, *Semiconductor Science and Technology*, 2005, **20**, 398–401.

17 B. Balamurugan and B. R. Mehta, *Thin Solid Films*, 2001, **396**, 90–96.

18 F. Marabelli, G. B. Parravicini and F. Salghetti-Drioli, *Physical Review B*, 1995, **52**, 1433–1436.

19 M. T. . Nair, L. Guerrero, O. L. Arenas and P. . Nair, *Applied Surface Science*, 1999, **150**, 143–151.

20 S. C. Ray, *Solar Energy Materials*, 2001, **68**, 307–312.

21 C. E. Ekuma, V. I. Anisimov, J. Moreno and M. Jarrell, *The European Physical Journal B*, 2014, **87**, 23.

22 M. Dahrul, H. Alatas and Irzaman, *Procedia Environmental Sciences*, 2016, **33**, 661–667.

23 J. F. Pierson, A. Thobor-Keck and A. Billard, *Applied Surface Science*, 2003, **210**, 359–367.

24 G. V. Samsonov, *The Oxide Handbook*, IFI/Plenum, New York, 1973.

25 A. L. Edwards, *A Compilation Of Thermal Property Data For Computer Heat-Conduction Calculations*, Report No. UCRL-50589, 1969.

26 Y. S. Gong, C. Lee and C. K. Yang, *Journal of Applied Physics*, 1995, **77**, 5422–5425.

27 A. S. Tremsin, O. H. Siegmund, J. S. Hull, J. V. Vallerga, J. B. McPhate, J. Soderstrom, J.-W. Chiou, J. Guo and Z. Hussain, *IEEE Nuclear Science Symposium Conference Record*, 2006, **2**, 735–739.

28 S. Poulston, P. M. Parlett, P. Stone and M. Bowker, *Surface and Interface Analysis: An International Journal devoted to the development and application of techniques for the analysis of surfaces, interfaces and thin films*, 1996, **24**, 811–820.

29 M. Heinemann, B. Eifert and C. Heiliger, *Physical Review B*, 2013, **87**, 115111.

30 P. Jiang, D. Prendergast, F. Borondics, S. Porsgaard, L. Giovanetti, E. Pach, J. Newberg, H. Bluhm, F. Besenbacher and M. Salmeron, *The Journal of Chemical Physics*, 2013, **138**, 024704.

31 S. Eisebitt, T. Böske, J.-E. Rubensson and W. Eberhardt, *Physical Review B*, 1993, **47**, 14103–14109.

32 D. Tahir and S. Tougaard, *Journal of Physics: Condensed Matter*, 2012, **24**, 175002.

33 W. K. C. Yung, B. Sun, Z. Meng, J. Huang, Y. Jin, H. S. Choy, Z. Cai, G. Li, C. L. Ho, J. Yang and W. Y. Wong, *Scientific Reports*, 2016, **6**, 39584.

34 CuO - X-ray attenuation length, http://henke.lbl.gov/optical_constants/atten2.html, (accessed 28 November 2018).

35 H. E. Elsayed-Ali and J. W. Herman, *Applied Physics Letters*, 1990, **57**, 1508–1510.

36 J. H. Bechtel, *Journal of Applied Physics*, 1975, **46**, 1585–1593.

37 J. Crank, *The Mathematics of Diffusion*, Oxford University Press, Oxford, England, second., 1975.

38 copper oxide - National Insitute for Standards and Technology, https://webbook.nist.gov/cgi/cbook.cgi?ID=C1317380&Type=JANAFS&Table=on, (accessed 28 November 2018).
39 P. J. Cumpson and M. P. Seah, *Surface and Interface Analysis*, 1992, **18**, 345–360.
40 M. Liu, M. Lin and C. Wang, *Nanoscale Research Letters*, 2011, **6**, 297.
41 D. Anandan and K. S. Rajan, *Asian J. Sci. Res.*, 2012, **5**, 218–227.

Laser-induced energy deposition and heat transport in CuO is studied by picosecond time-resolved X-ray absorption spectroscopy

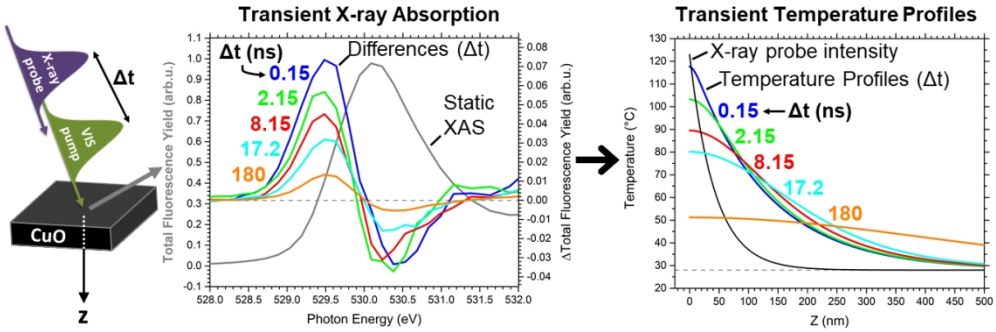
X-ray probe
VIS pump
Δt
CuO
z
Transient X-ray Absorption
Δt (ns)
0.15
2.15
8.15
17.2
180
Differences (Δt)
Static XAS
Total Fluorescence Yield (arb.u.)
ΔTotal Fluorescence Yield (arb.u.)
Photon Energy (eV)
Transient Temperature Profiles
X-ray probe intensity
Temperature Profiles (Δt)
0.15 ← Δt (ns)
2.15
8.15
17.2
180
Temperature (°C)
Z (nm)